scientific reports

Check for updates

OPEN

Impact of *LIN7A* silencing on U87 cell invasion and its clinical significance in glioblastoma

Xiaojuan Lyu[1], Yuxiang Shi[2], Daixu Wang[3], Xing Cao[1], Jipeng Guo[1], Guodong Huang[1], Lin Zhou[4], Mengxian Zhang[5] & Zhen Dong[6✉]

Glioblastoma is highly aggressive and resistant to treatment, making it crucial to understand the regulatory mechanisms underlying its invasion. LIN7A, a polar protein, has been implicated in tumor cell migration and invasion, but its role in glioblastoma remains unclear. This study aimed to manipulate *LIN7A* gene expression in U87 cells, analyze its impact on invasion, and explore the potential mechanisms through which LIN7A regulates glioblastoma cell invasion. Lentiviral vectors were used to silence the *LIN7A* gene in U87 cells, selecting the most effective vector. *LIN7A* gene transcription, protein expression and localization were analyzed using RT-qPCR, Western blotting, and immunofluorescence. U87 cell invasion was assessed via real-time cell analysis and spheroid invasion assay, while MMP-2 and MMP-9 protease activities were measured using zymography. β-catenin protein levels and localization were evaluated through Western blotting and immunofluorescence. Expression of target genes in the β-catenin pathway was also measured. An orthotopic xenograft glioblastoma model in nude mice was established by intracranial implantation of U87 cells, with tumor growth monitored using immunofluorescence analysis of brain slices. The clinical significance of *LIN7A* expression was confirmed by comparing its levels in core and peripheral invading areas of glioblastoma and analyzing RNASeq data and clinical information from the Clinical Proteomic Tumor Analysis Consortium (CPTAC) GBM cohort. Transfection of U87 cells with a lentiviral vector led to decreased LIN7A levels and altered distribution patterns. Silencing the *LIN7A* gene increased U87 cell proliferation and invasiveness, reduced clonal formation ability, and enhanced MMP-2 and MMP-9 protease activity. It also resulted in a slight increase in cytoplasmic β-catenin content, although not statistically significant, but a significant increase in nuclear β-catenin accumulation and transcriptional activity of target genes in the pathway. Animal studies showed that *LIN7A* gene silencing caused U87 cells to transition from clumpy to invasive growth mode. LIN7A expression was significantly lower in the peripheral invading area compared to the core area in clinical samples of glioblastoma. Data mining of the CPTAC-GBM cohort revealed a strong association between *LIN7A* gene expression and survival time. Silencing *LIN7A* may promote U87 tumor cell invasion by disrupting intercellular junctions, altering cell polarity, and activating the β-catenin pathway. Further research is warranted to elucidate the role of LIN7A in glioblastoma cell invasion.

Keywords Glioblastoma, Cell invasion, *LIN7A*, β-catenin

Glioblastoma stands as the most prevalent malignant primary brain tumor, constituting approximately 57% of all gliomas and 48% of all primary malignant central nervous system tumors. Despite advancements in standard therapy, patients face grim prognoses, with a median survival of less than two years[1]. Recurrence, driven by glioblastoma cell infiltration into healthy brain tissue, is a persistent challenge. Anti-angiogenic therapies may

[1]Department of Oncology, Wuhan Centre Hospital, Wuhan 430024, People's Republic of China. [2]Department of Pathology, Wuhan Centre Hospital, Wuhan 430024, People's Republic of China. [3]Department of Neurosurgery, Wuhan Centre Hospital, Wuhan 430024, People's Republic of China. [4]Department of Histoembryology, Tongji Medical College, Huazhong University of Science and Technology, Wuhan 430030, People's Republic of China. [5]Department of Oncology, Tongji Hospital, Tongji Medical College, Huazhong University of Science and Technology, Wuhan 430030, People's Republic of China. [6]Department of Neurosurgery, Tongji Hospital, Tongji Medical College, Huazhong University of Science and Technology, Wuhan 430030, People's Republic of China. ✉email: dongz@tjh.tjmu.edu.cn

1

even exacerbate tumor aggressiveness in glioblastoma[2–5], highlighting the need to understand the mechanisms of invasiveness for improved therapies.

Cancer cell invasion involves alterations in cell polarity and signaling pathways. While quiescent cells exhibit apical-basal polarity, migratory cells shift to anterior–posterior polarity[6–10]. This polarity transition, associated with epithelial-mesenchymal transition (EMT), is critical in tumor invasiveness. EMT disrupts cell polarity and adhesion, promoting pro-migratory gene expression and cytoskeletal changes[11,12]. Polarity proteins, key regulators of cell signaling and cytoskeletal dynamics, can be co-opted by tumor cells to drive invasion[13].

Three conserved polarity complexes—PAR, Crumbs, and SCRIB—maintain apical-basal polarity and inhibit EMT and metastasis. Their disruption is linked to enhanced tumor invasion via pathways like Rho GTPase signaling and loss of cell–cell adhesion[14–20]. Evidences suggest that maintaining epithelial cell polarity serves as a protective barrier against cancer, while the dysregulation of polarity complexes can lead to increased cancer cell invasiveness and metastasis.

The LIN7 protein family, a component of the Crumbs polarity protein complex, has been shown to regulate tumor cell migration and invasion in melanoma[21] and squamous epithelial cell carcinoma[22]. However, its role in glioma remains largely unexplored. This study investigates the role of LIN7A in U87 glioblastoma invasion, its potential regulatory mechanisms, and the clinical relevance of LIN7A expression.

Materials and methods
Glioblastoma cells and culture conditions
Glioblastoma cell line U87 was obtained from the American Type Culture Collection (ATCC). Cells were grown in Dulbecco's modified Eagle's medium (DMEM), supplemented with 1% glutamine, 100 µg/mL streptomycin, 100 U/mL penicillin, and 10% fetal calf serum. They were maintained in a humidified atmosphere containing 5% CO_2 at 37 °C.

Knockdown of gene expression
LIN7A was silenced using lentiviral particles with short hairpin RNA (shRNA) constructs (Mission® shRNA, Sigma). Five individual sequences cloned in pLKO.1-puro vectors were lentiviral-transduced into U87 cells with the addition of 8 µg/mL of Polybrene. Cells were selected using puromycin at a concentration of 2 µg/mL. Knockdown efficacy was confirmed using quantitative real-time polymerase chain reaction (RT-qPCR). The non-targeting shRNA lentiviral construct (Mission® SHC002, Sigma) was used as a control. 'U87sh*LIN7A*' represents U87 cells with *LIN7A* gene silencing, while 'U87 Ctrl' represents control cells.

Quantitative real-time PCR
Total RNA extraction was carried out using an RNA purification system (Qiagen), followed by treatment with RNase-free DNase I to eliminate genomic DNA contamination (Roche). Subsequently, cDNA synthesis was performed using Superscript RNase H-Reverse Transcriptase (Invitrogen) and random hexamers (Sigma-Aldrich) with 5 µg of total RNA. Gene expression analysis was conducted in triplicate using the ABI Prism 7000 Sequence Detection System (Applied Biosystems) and SYBR Green Master Mix (Eurogentec). Standard curves were generated for each transcript, demonstrating amplification efficiency ranging from 90 to 100%. Relative quantification of gene expression was determined by comparing threshold values, with all results normalized to glyceraldehyde-3-phosphate dehydrogenase (GAPDH) as a housekeeping gene. Primers were procured from Sigma-Aldrich, and the primer sequences can be found in Table 1.

Western blot analysis
To assess protein expression levels in whole cells, cell pellets were harvested and mechanically homogenized in lysis buffer containing 50 mM Tris–HCl (pH 7.4), 50 mM NaCl, 1% Triton X-100, 1 mM EDTA, 20 mM NaF, 2 mM Na_3VO_4, 1 mM PMSF, and 1 µg/ml each of aprotinin, leupeptin, and pepstatin. The homogenates were then clarified by centrifugation at 14,000*g* for 15 min at 4 °C, and total protein extracts were obtained from the supernatant. Nucleoprotein and cytoplasmic protein from cultured U87 cells were extracted according to the

Target	Forward primer	Reverse primer
LIN7A	5′-GCAACAGCAAAGGCAACAGT-3′	5′-CTCTTTTGAGGCCTCCGTGT-3′
VEGF	5′-CTACCTCCACCATGCCAAGT-3′	5′-GCAGTAGCTGCGCTGATAGA-3′
FZD7	5′-CAGACGTGCAAGAGCTATGC-3′	5′- ACGATCATGGTCATCAGGTACT-3′
TCF1	5′-CAGAGGAGAGGAACCAAGCTA-3′	5′-GCAACTCGGGACATAAAGCC-3′
CD44	5′-TTTGCATTGCAGTCAACAGTC-3′	5′-GTTACACCCCAATCTTCATGTCCAC-3′
MMP2	5′-TCTCCTGACATTGACCTTGGC-3′	5′-CAAGGTGCTGGCTGAGTAGATC-3′
MMP7	5′-GAGTGAGCTACAGTGGGAACA-3′	5′-CTATGACGCGGGAGTTTAACAT-3′
C-MYC	5′-TCATCCAGGACTGTATGTGGAG-3′	5′-GTAGGAGGCCAGCTTCTCTG-3′
CYCLIN D1	5′-GAGGAAGAGGAGGAGGAGGA-3′	5′-GAGATGGAAGGGGGAAAGAG-3′
MMP9	5′-TTGACAGCGACAAGAAGTGG-3′	5′-GCCATTCACGTCGTCCTTAT-3′
GAPDH	5′-TGAGCGATGTGGCTCGGCT-3′	5′-CTCTCTGCTCCTCCTGTTCGAC-3′

Table 1. The primers used in RT-qPCR.

Antibody type	Specificity	Dilution	Catalog number	Supplier
Primary antibody	Anti-LIN7A (rabbit polyclonal)	WB 1:1000 IF 1:500	PA5-30871	Invitrogen
Primary antibody	Anti-beta-catenin (rabbit polyclonal)	WB 1:4000 IF 1:2000	ab6302	Abcam
Primary antibody	Anti-lamin B1 (rabbit polyclonal)	WB 1:1000	ab16048	Abcam
Primary antibody	Anti-alpha tubulin (rabbit monoclonal)	WB 1:1000	ab52866	Abcam
Primary antibody	Anti-human nestin (rabbit polyclonal)	IF 1:200	ZRB69	MilliporeSigma
Primary antibody	Anti-isocitrate dehydrogenase 1 (IDH1)-R132H (mouse monoclonal)	IF 1:500	SAB4200548	Merck
Secondary antibody	Alexa fluor 488 goat anti-rabbit IgG (H + L)	IF 1:500	A-11008	Invitrogen
Secondary antibody	Alexa fluor 594 goat anti-mouse IgG (H + L)	IF 1:500	A-11005	Invitrogen

Table 2. The detailed information of antibodies used in this study.

instructions provided by Proteintech (Cat No: PK10014). Protein concentration was determined using the BCA method.

Next, proteins (100 μg of total protein per well) were separated by 10% SDS-PAGE and subsequently electro-transferred onto nitrocellulose membranes. The membranes were blocked in 5% fat-free milk with 0.05% Tween*-20 for 1 h at room temperature with constant agitation, followed by overnight incubation with primary antibodies at 4 °C. Protein visualization was achieved using an enhanced chemiluminescence detection system. For detailed information regarding the antibodies, please refer to Table 2.

Zymography

Cells were treated as indicated above and cultured in serum-free medium for 24 h. The supernatant was harvested, and soluble protein was condensed. For each type of cell, 20 μg of protein was separated by 10% SDS-PAGE containing 0.1% gelatin without denaturing agents. Gels were washed twice for 30 min in 50 mM Tris–HCl (pH 7.5) and 2.5% Triton X-100. Subsequently, they were incubated overnight at 37 °C in a solution containing 50 mM Tris–HCl (pH 7.6), 10 mM $CaCl_2$, 150 mM NaCl, and 0.05% NaN_3 to allow the gelatinases to digest the gelatin structure. Finally, gels were stained with Coomassie Brilliant Blue R-250 and destained with a mixture of 90% methanol and water (1:1) and 10% glacial acetic acid. Bright bands indicative of gelatinolytic activity were observed at Mr 92,000 for MMP-9 and Mr 72,000 for MMP-2.

Limiting dilution assay

The clonogenic potential of glioblastoma cells was evaluated using the Limiting Dilution Assay. Four different dilutions (300 cells per well, 50 cells per well, eight cells per well, and one cell per well) were seeded in a 96-well plate, with 24 wells per dilution, and cultured for 28 days. The number of wells with colony formation was counted. The resulting data were tabulated, and an online tool was employed to assess differences in clonal formation potential between the two cell types[23].

Real-time cell analysis

Real-time cell analysis (RTCA) of cell proliferation and invasion was conducted using the xCELLigence DP device (Roche Diagnostics) following the manufacturer's instructions[24]. For cell proliferation assessment, E-Plates were utilized. Logarithmic phase cells were harvested at suspension concentrations of 2.5×10^4/mL and 4×10^4/mL. Initially, 150 μL of medium was added, and the background impedance value was recorded once equilibrium was reached. Subsequently, 100 μL of each cell suspension was added to four wells for each cell concentration. Culture assays began once the cells settled and equilibrated. To evaluate cell invasiveness, the bottom side of the wells in the upper chamber of the CIM-Plate was coated with 30 μl of collagen I (400 μg/ml, Sigma), and the surface of the upper chamber was covered with a monolayer of 5% (v/v) growth factor-reduced matrigel (BD Biosciences), diluted 1:20 with basal medium as specified by Roche in the application notes. Next, 25,000 cells/well suspended in culture medium without FBS were seeded in the upper chambers, while the lower chambers were filled with full medium containing FBS. The dimensionless cell index (CI), derived as a relative change in measured electrical impedance caused by migrated cells, served to reflect the invasive behavior of monitored cells. Cell indices were measured every 15 min for up to 24 h using the RTCA software (version 1.2).

Three-dimensional (3D) tumor spheroid invasion assay

This assay was performed following previously established protocols[25]. Briefly, U87 cells were seeded in ultra-low attachment 96-well plates (Corning Life Sciences, USA) at a density of 2500 cells/well. The cells were then incubated at 37 °C with 5% CO_2 for 72 h to allow for the formation of 3D spheroids. Flat-bottom 96-well plates were coated with 125 μg/ml growth factor–reduced Matrigel (Corning) in culture medium lacking growth factors and incubated for 2 h at room temperature. Once coating was complete, a single spheroid per well was transferred onto the Matrigel-coated plates. The spheroids were then cultured in a mixture of medium and Matrigel. Microscopic images of the area covered by each spheroid were captured at 0, 24, 48, and 72 h after implantation. For quantification, the mean area covered by invaded glioblastoma cells at each time point was measured in 24-h intervals and compared to the area at 0 h. Changes in sphere area over time were analyzed using ImageJ. Invasiveness over time was graphically represented, and statistical differences between groups were determined.

Xenograft mouse model

All procedures on mice presented in this manuscript complied with the Hubei Provincial Regulations on Laboratory Animal Administration and the guidelines of the Laboratory Animal Ethics Committee of Huazhong University of Science and Technology (HUST), receiving formal approval from the Laboratory Animal Ethics Committee of Tongji Medical College, HUST. Reporting in this manuscript follows the recommendations of the ARRIVE guidelines[26].

Female athymic mice (CD1 nu/nu), aged 6 to 12 weeks, were sourced from the Experimental Animal Center of Tongji Medical College, Huazhong University of Science and Technology (Wuhan, China). These mice were bred in specific pathogen-free rooms to maintain their health status.

This study involved two groups of mice, with each group consisting of four animals. Mice were anesthetized via intraperitoneal injection of 100 mg/kg ketamine and 10 mg/kg xylazine[27]. Each group received stereotactic implantation of either 1×10^5 U87sh*LIN7A* or U87Ctrl cells into the right striatum. At 3- and 4-weeks post-implantation, the mice were euthanized humanely through an overdose of inhalant anesthetic, followed by cervical dislocation, and their brains were carefully removed and cryosectioned for further analysis.

The experimental protocol complied with the Hubei Provincial Regulations on Laboratory Animal Administration and the guidelines of the Laboratory Animal Ethics Committee of Huazhong University of Science and Technology (HUST), receiving formal approval from the Laboratory Animal Ethics Committee of Tongji Medical College, HUST.

Glioblastoma tissue specimens

Glioblastoma tissue specimens were obtained and promptly cryopreserved using liquid nitrogen. These specimens were collected from patients diagnosed with glioblastomas and treated at Tongji Hospital, affiliated with Tongji Medical College, Huazhong University of Science and Technology, between June and December 2022. To facilitate the identification of tumor cells in immunofluorescence assays, only cases of glioblastoma positive for the IDH1R132H mutation were selected for inclusion. All patients provided informed consent. This study was approved by the Committee on Human Research of Tongji Hospital. All methods were performed in accordance with the relevant guidelines and regulations, as approved by the Committee on Human Research of Tongji Hospital.

Immunofluorescence

Cells were cultured on glass coverslips pre-coated with collagen I. When reaching 70% confluency, cells were fixed with 2% paraformaldehyde in phosphate-buffered saline (PBS) for immunofluorescence staining. Following fixation, cells were permeabilized with 0.3% Triton-X100 in PBS for 5 min and then incubated with primary antibodies diluted in 5 mg/ml bovine serum albumin (BSA) in PBS for 4 h at room temperature. Subsequently, cells were washed with PBS containing Tween 20 (PBST) and incubated with secondary antibodies diluted in 1% BSA in PBST for 1 h at room temperature in the dark. After three washes with PBST in the dark, cells were counterstained with 500 nM Propidium Iodide (PI) for 5 min at room temperature and mounted with mounting medium. Immunofluorescence images were acquired using a Cell Observer microscope (Zeiss). For detailed information regarding the antibodies, please refer to Table 2.

For mouse xenografts, immunofluorescence staining was performed using rabbit anti-human nestin antibody after cryosections were fixed with acetone. Alexa Fluor™ 488 anti-rabbit antibody was utilized as the secondary antibody. To visualize whole brain slices, images were automatically taken on Cell Observer (Zeiss) in high-magnification mosaic mode (Zeiss MosaiX), managed by ZEN software.

For glioblastoma tissue specimens, immunofluorescence staining on frozen sections of clinical samples was performed. Detailed antibody information is provided in Table 2. For each sample, two-channel fluorescence images of the tumor core and the invasive margin were obtained using Cell Observer (Zeiss). ImageJ software was employed to select the region of interest (ROI) by setting a threshold for the IDH fluorescence channel. Subsequently, the average fluorescence intensity of the LIN7A channel was calculated to facilitate statistical analysis of the differences between groups.

Clinical survival analysis

To evaluate the prognostic significance of LIN7A in glioblastoma, RNASeq data and clinical information from the Clinical Proteomic Tumor Analysis Consortium Glioblastoma (CPTAC-GBM) cohort were obtained via the Genomic Data Commons (GDC) data portal. Processed data at level 3 were utilized for analysis. Samples were stratified into two groups based on *LIN7A* expression levels. High and low *LIN7A* expression per sample was determined relative to the median expression of this gene within the cohort.

Overall survival probability curves were generated using the Kaplan–Meier method, and differences between the curves were assessed using the log-rank test[28]. Additionally, the relationship between *LIN7A* expression and progression-free survival was evaluated using Spearman's rank correlation analysis[29].

Statistical analyses

Quantitative data for mRNA expression were obtained using RT-qPCR, zymography, and Western blot as described earlier. The experiments were repeated three times, and statistical analyses were conducted and visualized using SigmaPlot 12.5. The data are presented as mean ± standard deviation (SD). Statistical analysis for clone formation experiments was carried out using online tools (http://bioinf.wehi.edu.au/software/elda). RTCA data analyses utilized the built-in software RTCA software 1.2. Clinical Survival Analyses were conducted using R packages, specifically 'survival' and 'corr'. All tests were performed at the 0.05 level of significance.
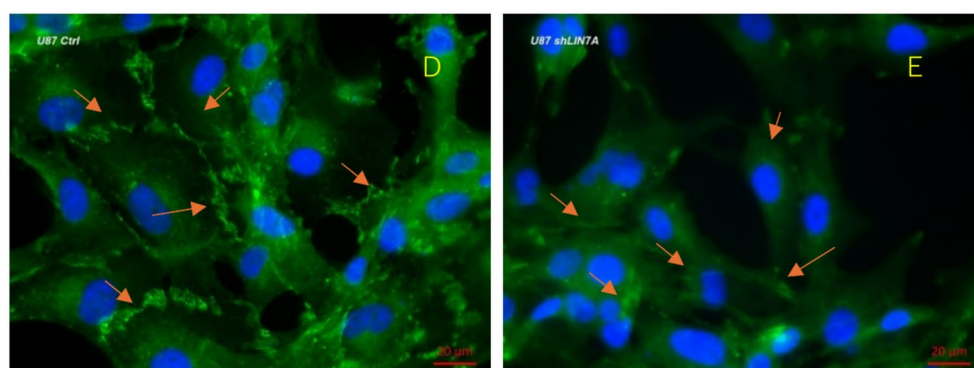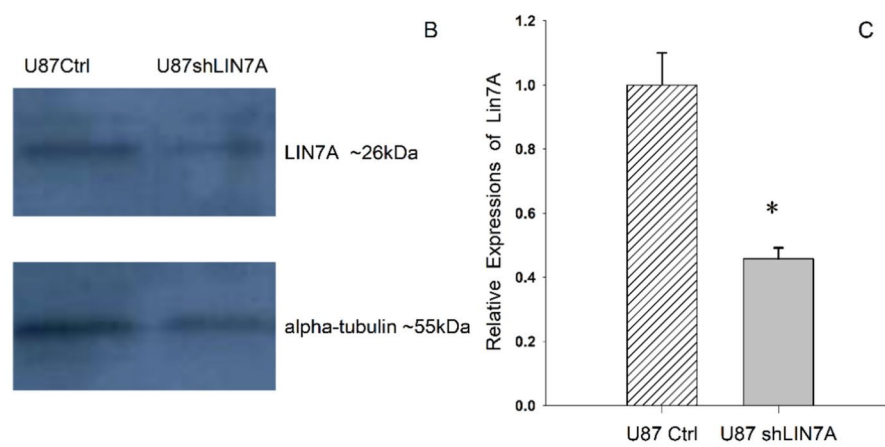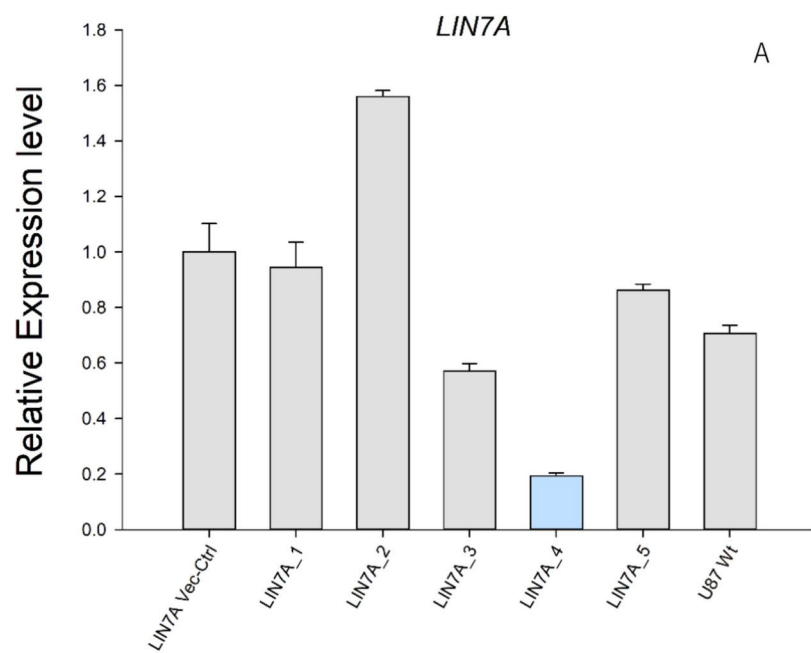
◄**Fig. 1**. *LIN7A* gene silencing and validation. (**A**) Design of lentiviral vectors for *LIN7A* gene silencing: five distinct lentiviral vectors were designed to target the *LIN7A* gene, with corresponding empty vectors serving as controls. These vectors were used to transfect U87 cells at two different multiplicities of infection (MOIs), 1:10 and 1:100. The efficacy of gene silencing was assessed using quantitative reverse transcription polymerase chain reaction (RT-qPCR), which allowed for the selection of the most effective vector. The selected vector's clone ID is NM_004664.2-710s1c1 (TRCN0000116870-CCGGGAACTACTCAAGGCTGCTAAACTCGAGT TTAGCAGCCTTGAGTAGTTCTTTTTG). (**B**) Western blotting for confirmation of *LIN7A* gene silencing: western blot analysis was performed to confirm the efficiency of *LIN7A* gene silencing. The LIN7A protein band appeared at approximately 26 kDa, while the α-tubulin band, used as a loading control, was observed at 55 kDa. (**C**) Quantitative analysis of LIN7A expression: quantitative analysis of the western blot bands was conducted using ImageJ software. The analysis revealed a significantly higher intensity of the LIN7A band in U87Ctrl cells compared to U87sh*LIN7A* cells (*$P < 0.05$), confirming the successful silencing of *LIN7A* in U87sh*LIN7A* cells. (**D**,**E**) Immunofluorescence staining of *LIN7A* protein expression: immunofluorescence staining was performed to visualize LIN7A protein expression in U87 cells. In U87Ctrl cells (**D**), LIN7A protein was primarily localized to cell junctions, as indicated by green staining, while nuclei were stained blue. In contrast, LIN7A expression was significantly reduced and lost its typical localization in U87sh*LIN7A* cells (**E**), confirming successful gene silencing at the protein level. Additionally, as indicated by the yellow arrows, the cell junctions in U87Ctrl cells were intact, whereas those in U87sh*LIN7A* cells appeared unclear, suggesting disruption and compromised integrity of the cell junctions.

Results
LIN7A gene silencing alters its protein expression and distribution pattern
The most effective shRNA construct was identified through RT-qPCR and subsequently chosen for the subsequent experiments (Fig. 1A). Western blotting analysis revealed a significant reduction in LIN7A protein expression in U87sh*LIN7A* cells compared to the control group (Fig. 1B, C). Furthermore, cellular immunofluorescence analysis demonstrated that U87Ctrl cells exhibited strong fluorescence intensity of LIN7A, localized predominantly at cellular junctions. Conversely, in U87sh*LIN7A* cells, the fluorescence intensity of LIN7A was notably decreased, and its distribution no longer showed the characteristic concentration at the cell membrane and junctions. Instead, LIN7A displayed a disordered distribution across the cell membrane and cytoplasm. The cell junctions in U87Ctrl cells were intact, whereas those in U87sh*LIN7A* cells appeared unclear, suggesting disruption and compromised integrity of the cell junctions. (Fig. 1D, E).

LIN7A gene silencing promotes cell proliferation and invasion but inhibits clonegenicity
Real-time cell analysis (RTCA) conducted using Roche's xCELLigence system revealed that the cell proliferation rate of U87sh*LIN7A* cells was significantly higher than that of the control U87Ctrl cells, regardless of the initial cell number conditions (Fig. 2A, B). RTCA analysis of cell invasion, akin to the Boyden chamber experiment but utilizing resistance variation, demonstrated a notable increase in U87sh*LIN7A* cell invasion compared to the control group (Fig. 2C). This method allowed continuous monitoring and intervention administration during the experiment. To depict cellular invasion more accurately, a 3D spheroid invasion experiment was conducted. Results showed a significant increase in U87sh*LIN7A* cell aggressiveness compared to U87Ctrl when considering the extracellular matrix surrounding the spheroid (Fig. 2D, E).

The impact of *LIN7A* gene suppression on clonogenic potential was assessed using the limiting dilution technique. Findings revealed that a minimum of 4.48 U87Ctrl cells were required for clone formation, whereas 52.38 U87sh*LIN7A* cells were needed, indicating a notable disparity between the two cohorts ($P < 0.01$). These results suggest that inhibition of the *LIN7A* gene in U87 cells led to a reduction in clone formation, as depicted in Fig. 2F.

LIN7A gene silencing activates β-catenin pathway
Immunofluorescence staining of β-catenin was performed on cultured cells, revealing its distribution primarily in the perinuclear and intranuclear regions of U87 Ctrl cells. In contrast, U87sh*LIN7A* cells exhibited intense intranuclear fluorescence, indicating an elevated presence of β-catenin in the nucleus. This altered distribution signifies the translocation of β-catenin protein into the nucleus, a crucial step in the activation of the Wnt-β-catenin classical pathway (Fig. 3A).

Subsequent quantification of β-catenin protein revealed no statistically significant disparity in the overall cellular β-catenin protein content between U87sh*LIN7A* and U87Ctrl cells, as determined by Western blotting. However, the analysis of β-catenin content within the nucleus of U87sh*LIN7A* cells revealed a significant increase in β-catenin protein levels compared to the control U87Ctrl cells($P < 0.05$) (Fig. 3B).

Activation of the β-catenin pathway is typically accompanied by the upregulation of transcription of downstream target genes. RT-qPCR analysis was conducted to determine the transcription levels of AXIN2, CD44, FZD7, TCF1, MMP2, and MMP9 genes. The findings revealed that all target genes were transcriptionally upregulated to varying extents in U87sh*LIN7A* cells, suggesting that *LIN7A* gene silencing might enhance the activity of the β-catenin classical pathway (Fig. 3C).

To assess changes in protein function, gelatin enzyme profiling was performed to measure MMP-2 and MMP-9 activity. Clear bands of different intensities indicating enzyme activity were observed. ImageJ software quantified transparency intensity, showing increased protease activity of MMP-2 and MMP-9 in U87sh*LIN7A* cells compared to U87Ctrl cells ($P < 0.05$) (Fig. 3D).
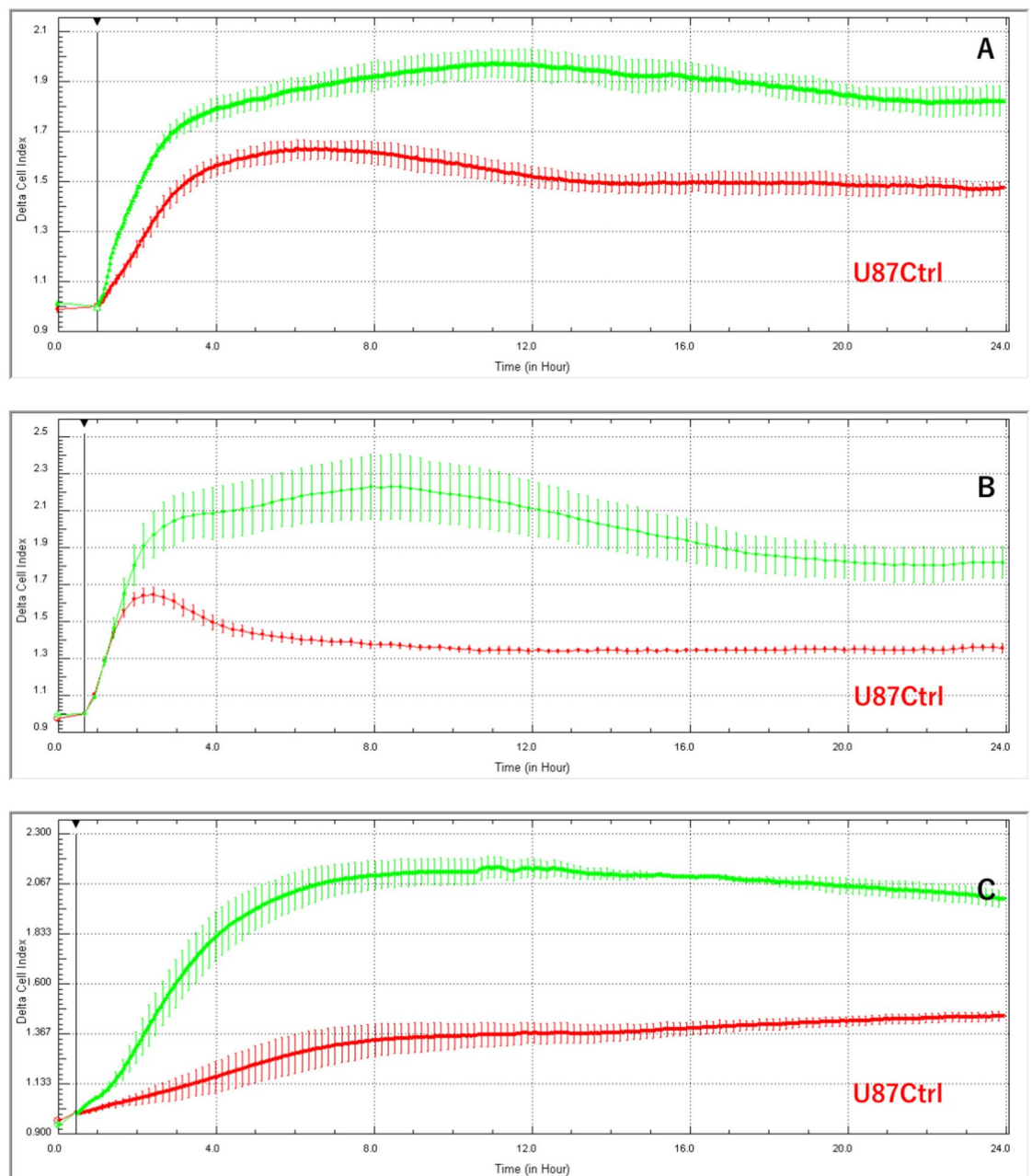
Fig. 2. Impact of *LIN7A* gene silencing on U87 cell proliferation, invasion, and clone formation. Impact of *LIN7A* silencing on U87 cell growth. The RTCA proliferation assay was performed by seeding cells onto E-plate plates at initial densities of 2500 cells (**A**) and 4000 cells (**B**). Cell proliferation was monitored over 24 h, and the growth curves of U87sh*LIN7A* (green) and U87Ctrl (red) were compared. Statistical analysis indicated a significant difference between the two groups ($P < 0.05$). *LIN7A* silencing enhances U87 cell invasion. The RTCA invasion assay (**C**) was performed using CIM-plate plates to evaluate and compare the invasion profiles of U87sh*LIN7A* (green) and U87Ctrl (red) cells. The analysis revealed a statistically significant difference between the two invasion curves ($P < 0.05$).For the spheroid invasion assay (**D**), 3D invasion of U87 spheroids into the brain-mimicking matrix (BMM) was monitored over time. Phase contrast microscopy images were captured at 0, 24, 48, and 72 h of culture. The invasion areas were quantified using ImageJ software, and the data showed statistically significant differences between the two groups (**E**) (*$P < 0.05$). *LIN7A* gene silencing inhibits clonogenicity of U87 cells clonogenic assay (**F**): cells were seeded at varying concentrations in each well, cultured under standard conditions, and monitored for colony formation over a 14-day period. The number of colonies formed for each initial cell density was quantified (as shown in Supplementary Figure S1). Statistical analysis revealed a significant difference between the two groups, with U87Ctrl cells requiring a minimum of 4.48 cells to form colonies, compared to 52.38 cells for U87sh*LIN7A* cells ($P < 0.01$).
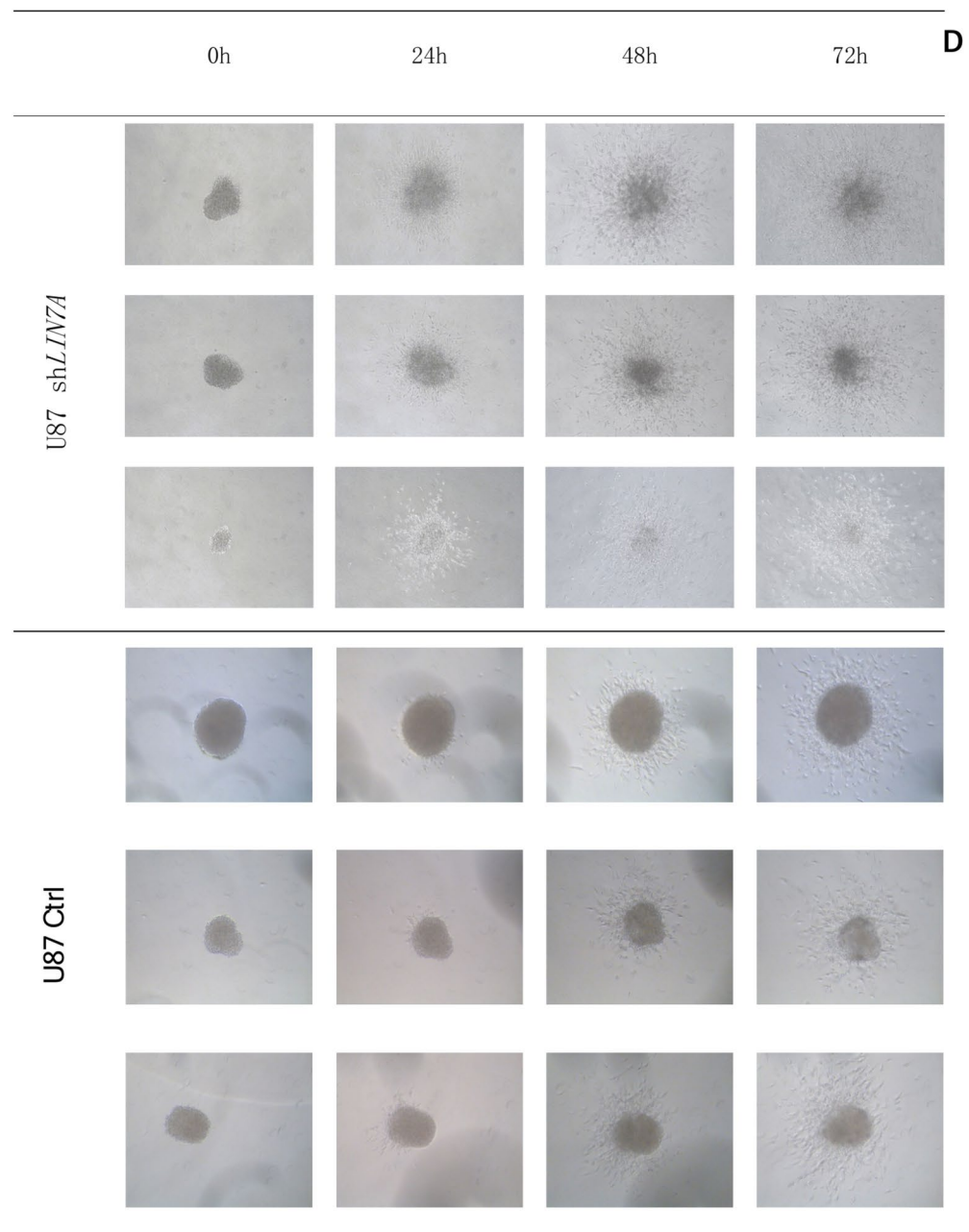
Figure 2. (continued)

LIN7A gene silencing changes U87 cells intracranial growth model

To explore the effect of *LIN7A* gene silencing on U87 cell invasiveness in vivo, we established a xenograft mouse model and monitored tumor growth patterns. By the third week, we observed that U87sh*LIN7A* cells exhibited a diffuse growth pattern and were smaller in size compared to the control group (U87Ctrl). In contrast, U87Ctrl cells displayed a clumpy growth pattern (Fig. 4A).

Moving to the fourth week, we noted multiple small satellite infiltrates surrounding the U87sh*LIN7A* tumor, while the U87Ctrl tumor maintained its clumpy growth (Fig. 4B). These findings indicate significant differences in the growth patterns of the two intracranial tumors at different time points. Notably, U87 cells following *LIN7A* gene silencing underwent a transition towards an infiltrative growth pattern.

LIN7A gene expression decreases in invading glioblastoma cells

To investigate the correlation between *LIN7A* gene expression and glioblastoma cell invasion, tissue samples were obtained from the central region of the GB tumor and the adjacent invasion zone during surgery, employing intraoperative navigation and intraoperative fluorescence tumor imaging technology. Immunofluorescence analysis revealed a pronounced cell density and abundant LIN7A protein expression within the core of the tumor, contrasting with the sparser distribution of tumor cells and absence of LIN7A protein expression in
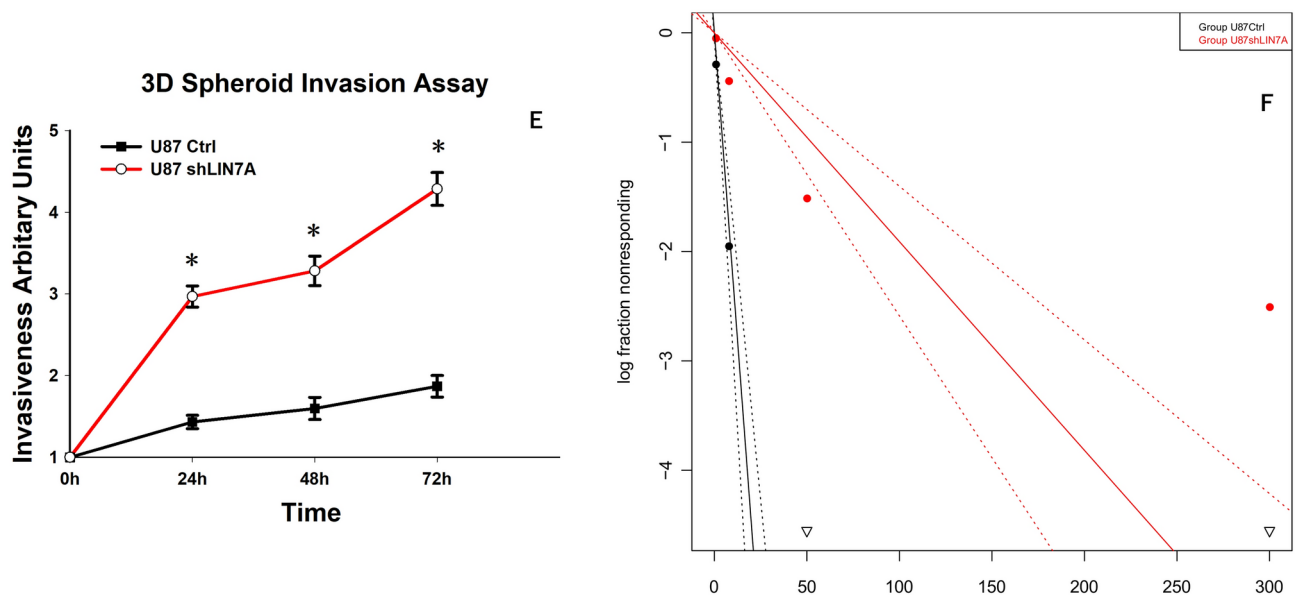
Figure 2. (continued)

the invasion zone (Fig. 5). Quantification of fluorescence intensity using Image J demonstrated a significant disparity between the two regions.

LIN7A gene expression correlates with survival time in CPTAC GBM cohort

Data mining of the CPTAC cohort validated the prognostic value of LIN7A in glioblastoma. The median overall survival (OS) time was significantly longer in the *LIN7A* high expression group compared to the low expression group (Fig. 6A). Kaplan–Meier analysis indicated a trend of longer median progression-free survival in the high *LIN7A* expression group compared to the low expression group, but the difference was not statistically significant.(Fig. 6B). Additionally, a moderate correlation was observed between *LIN7A* gene expression and progression-free survival (PFS) events (R = 0.24, P < 0.01) (Fig. 6C).

Discussion

Glioblastoma is highly aggressive, which is an important means of evading treatment and an important cause of treatment failure. Tumor invasion and cell polarity are closely related. Cell polarity, which is defined as asymmetry in cell shape, organelle distribution and cell function, is essential in numerous biological processes, including cell growth, cell migration and invasion, molecular transport, and cell fate[30]. Apical-basal polarity is typical of cells present in differentiated epithelium while front-rear polarity develops in motile cells[31]. In cancer development, the transition from epithelial to migratory polarity may be seen as the hallmark of cancer progression to an invasive and metastatic disease[32].

Despite the morphological and functional dissimilarity, both epithelial and migratory polarity are controlled by a common set of polarity complexes Par, Scribble and Crumbs[33]. The LIN7 protein, as an important component of Crumbs complex, plays a significant role in cell adhesion maturation. It consists of an L27 domain and a PDZ domain. The L27 domain plays a crucial role in mediating the interaction with CASK and is implicated in the assembly of multimeric complexes and the localization of LIN7A to cellular membranes[34]. Additionally, its PDZ domain facilitates binding with various proteins, thereby contributing to the maintenance of cell polarity, cell-to-cell adhesion junctions, and cell signaling processes[16].

The mechanisms by which cancer cells disrupt apical-basal polarity, leading to a migratory phenotype, remains an open question[35]. Oncogenic factors, along with the tissue microenvironment, activate pathways that suppress epithelial characteristics and promote invasive properties, known as epithelial-mesenchymal transition (EMT) in cancer progression. Cancer-related EMT disrupts cell polarity and adhesion, leading to increased expression of migration-promoting genes. This causes epithelial cells to lose connections and gain the ability to migrate away from the primary tumor site[36,37].

Studies conducted by Luo et al. (2018) and Gruel et al. (2016) have demonstrated that LIN7A promotes invasion in liver and breast cancer cells, indicating that its effects may be tumor type-specific[38,39]. However, glioblastomas exhibit significant biological differences from other epithelial-derived solid tumors, as they arise from glial cells rather than epithelial cells. Furthermore, their invasive characteristics are markedly distinct from those of other epithelial cancers. Our study revealed a disparity in *LIN7A* gene expression in glioblastoma, which is associated with tumor aggressiveness and consequently, patient prognosis. Analysis of the cohort demonstrated a significant elevation in LIN7A expression in tumor specimens from patients with extended overall survival (OS) compared to those with shorter OS. Furthermore, a positive correlation was observed between *LIN7A* expression and progression-free survival (PFS). Immunofluorescence analysis of distinct regions within the tumor sample (bulk vs. invading area) within the same case revealed a notable reduction in LIN7A protein
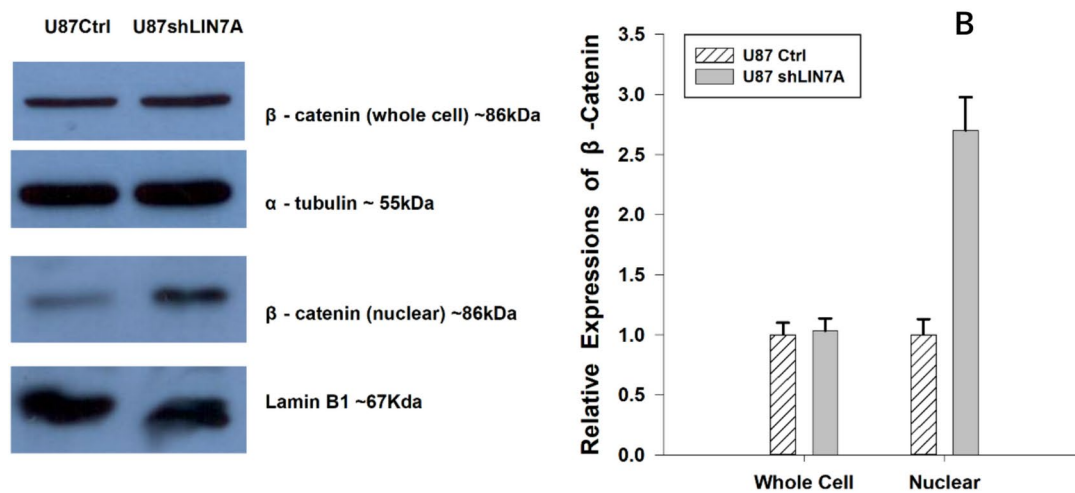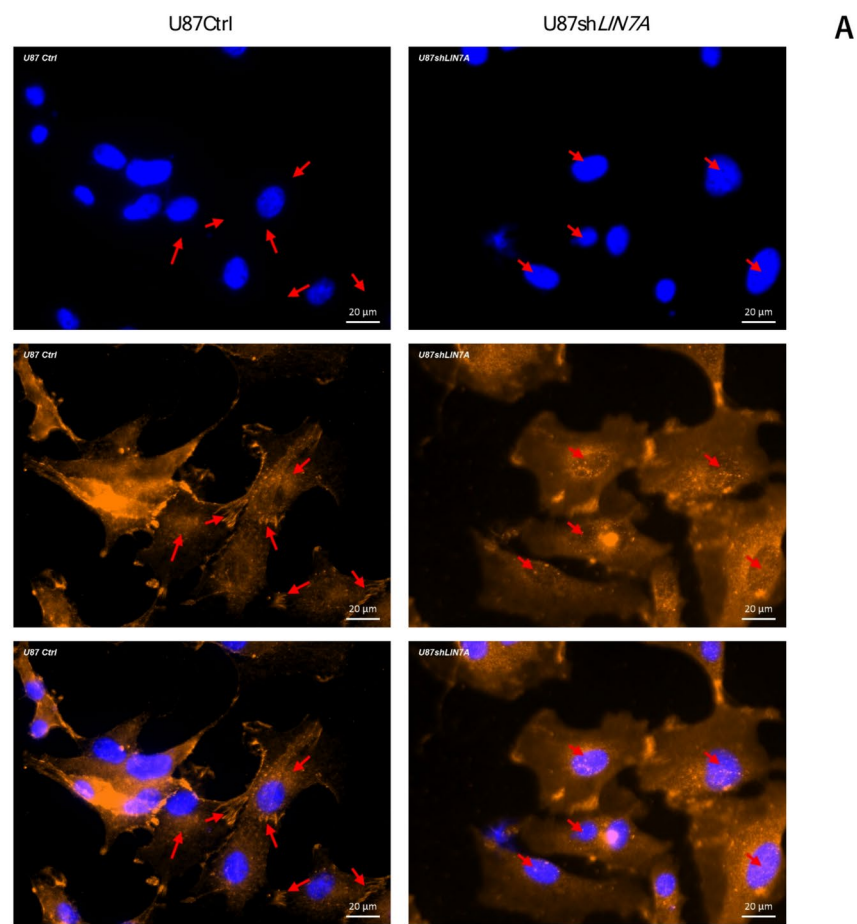
◀**Fig. 3.** *LIN7A* gene silencing activates β-catenin pathway. Immunofluorescence staining of β-catenin localization: immunofluorescence staining (**A**) was used to assess the intracellular distribution of β-catenin in U87sh*LIN7A* and U87Ctrl cells. U87sh*LIN7A* cells exhibited a notable increase in nuclear β-catenin content compared to U87Ctrl cells, as indicated by the red arrow, suggesting activation of the β-catenin pathway in response to *LIN7A* silencing. Western blotting analysis of β-catenin protein levels: western blot analysis (**B**) was performed to quantify β-catenin protein levels in whole-cell lysates and nuclear fractions. While there was no significant difference in total β-catenin protein content between U87sh*LIN7A* and U87Ctrl cells, a significantly higher level of nuclear β-catenin was observed in U87sh*LIN7A* cells (*$P < 0.05$). This indicates that *LIN7A* silencing promotes the nuclear translocation of β-catenin. RT-qPCR Analysis of β-catenin target gene transcription: RT-qPCR (**C**) was used to analyze the transcriptional activity of select target genes in the β-catenin pathway. U87sh*LIN7A* cells exhibited varying degrees of enhanced transcriptional activity of these genes compared to U87Ctrl cells (*$P < 0.05$, **$P < 0.01$), further confirming the activation of the β-catenin signaling pathway. Zymography of MMP-2 and MMP-9 activity: zymography (D) was utilized to quantify changes in MMP-2 and MMP-9 protease activity. U87sh*LIN7A* cells showed significantly higher levels of MMP-2 and MMP-9 activity compared to U87Ctrl cells (*$P < 0.05$), suggesting that β-catenin activation enhances protease activity involved in tumor invasion.

content in the invading area. Therefore, it is reasonable to speculate that the regulation of cell polar proteins by multiple signaling pathways of EMT may be an upstream mechanism for the decrease of *LIN7A* gene expression in invading glioblastoma cells.

To assess the expression of *LIN7A* in glioblastomas, we analyzed the transcription levels of *LIN7A* in various glioblastoma cell lines, including LN308, S24, U87, and T269 GIC[40], as well as in human astrocytes (Supplementary Figure S2). The U87 cell line was chosen as the representative model for our experiments due to its classic and well-documented characteristics. Our research demonstrates that silencing of the *LIN7A* gene in U87 cells results in a significant decrease in the content of the LIN7A polar protein, and more importantly, a notable change in its distribution, resulting in the breakdown of intercellular junctions and alteration of cell polarity. The loss of apical-basal polarity, characteristic of differentiated epithelial cells, is associated with the acquisition of a migratory phenotype in cells. As our results indicate that, compared to control U87Ctrl cells, U87sh*LIN7A* cells exhibited heightened aggressiveness both in vitro and in vivo, which can be attributed, at least in part, to the disruption of cell adhesion and altered cellular polarity. Moreover, we also conducted overexpression experiments on T269 GIC, a highly invasive cell line with low transcriptional levels of *LIN7A*, as mentioned earlier. The results showed that overexpressing *LIN7A* in T269 GIC partially inhibited its high invasiveness.

The disruption of tight junctions and adherens junctions leads to alterations in the localization of key apical proteins and transcriptional regulators, which can significantly impact gene transcription[41–44]. Specifically, the function of apical polarity proteins shifts from suppressing nuclear transcription to facilitating it. For example, the subcellular localization of ZO-1 protein varies between non-invasive and aggressive cells. In non-invasive cells, ZO-1 is primarily located in the plasma membrane, while in aggressive cells, it localizes to the nucleus[45]. Additionally, the disruption of the E-cadherin-catenin complex leads to the accumulation of β-catenin in the cytoplasm. This accumulation activates the Wnt signaling pathway, promoting cell proliferation and invasion once β-catenin translocate to the nucleus[46]. Experimental findings demonstrate that the LIN-7 PDZ protein engages in physical interactions with the PDZ target sequence of β-catenin, establishes an in vivo complex with the cadherin–β-catenin system, and facilitates adhesion processes linked to cadherin[47]. Moreover, research indicates a direct association between LIN-7 and the C-terminal PDZ binding sequence of the β-catenin protein in mammalian epithelial and neuronal cells, resulting in the formation of a LIN-7/cadherin/β-catenin complex[48]. The study by Monzani et al. further validated the interaction between LIN-7 and β-catenin in melanoma cells[21]. Recent findings suggest that LIN-7 binds to β-catenin and plays a role in regulating tumor invasion and metastasis in certain solid tumors: Onda et al. demonstrated that the downregulation of the LIN7C gene serves as a biomarker for metastasis in oral squamous cell carcinoma, as evidenced by proteomic analysis, functional validation, and clinical testing. Conversely, the upregulation of LIN7C gene in oral squamous cell carcinoma cells does not hinder cell proliferation, but rather induces a non-invasive cell phenotype and enhances the expression of β-catenin[49]. Additionally, Uzawa et al. utilized Miltazapine to facilitate the synthesis of LIN7C protein in squamous cell carcinoma and melanoma cells, leading to its interaction with β-catenin and subsequent inhibition of tumor metastasis[22].

The invasion of tumor cells is a dynamic process in which matrix metalloproteinases (MMPs) play a crucial role, along with the transition of cell polarity from epithelial to migratory and the degradation of extracellular matrix components. Our experimental findings demonstrate that silencing the *LIN7A* gene results in upregulation of MMP2 and MMP9 transcription levels, protein expression, and enzymatic activity in U87 cells. Given that MMP2 and MMP9 are downstream targets of the Wnt-β-catenin signaling pathway, we also investigated the impact of gene silencing on the transcriptional regulation of these target genes within the pathway, revealing variable degrees of upregulation. Additional analysis of the protein levels of β-catenin in the nucleus and cytoplasm revealed a slight increase in intracytoplasmic β-catenin content following gene silencing, although the difference was not statistically significant. In contrast, there was a significant increase in the nuclear β-catenin protein content.

Based on the findings of our experiment and other corroborating studies, it is plausible to hypothesize that the downregulation of the *LIN7A* gene and subsequent reduction in LIN7A protein levels may result in the liberation of cytosolic β-catenin and its translocation from the cell membrane to the nucleus. This process could
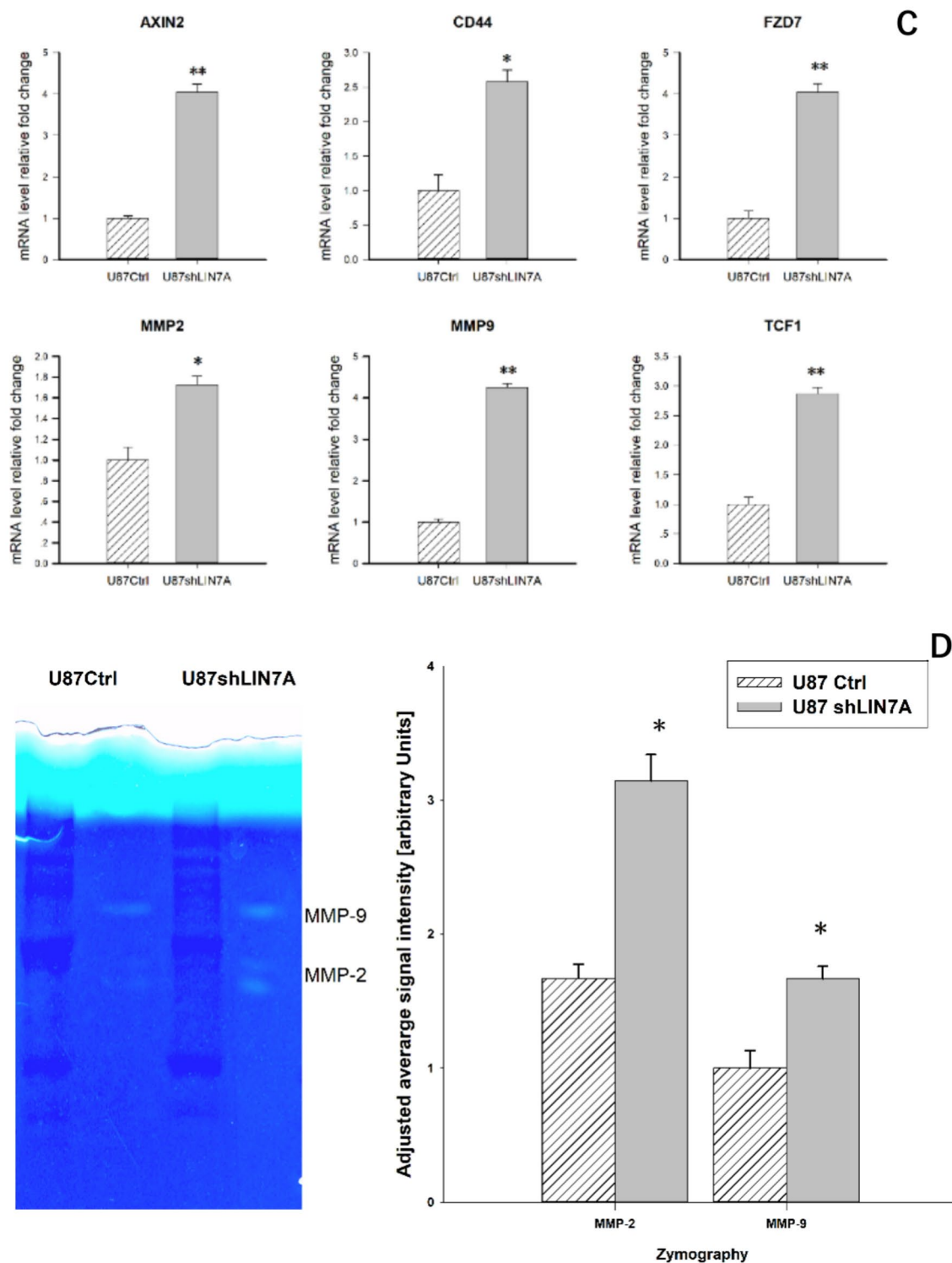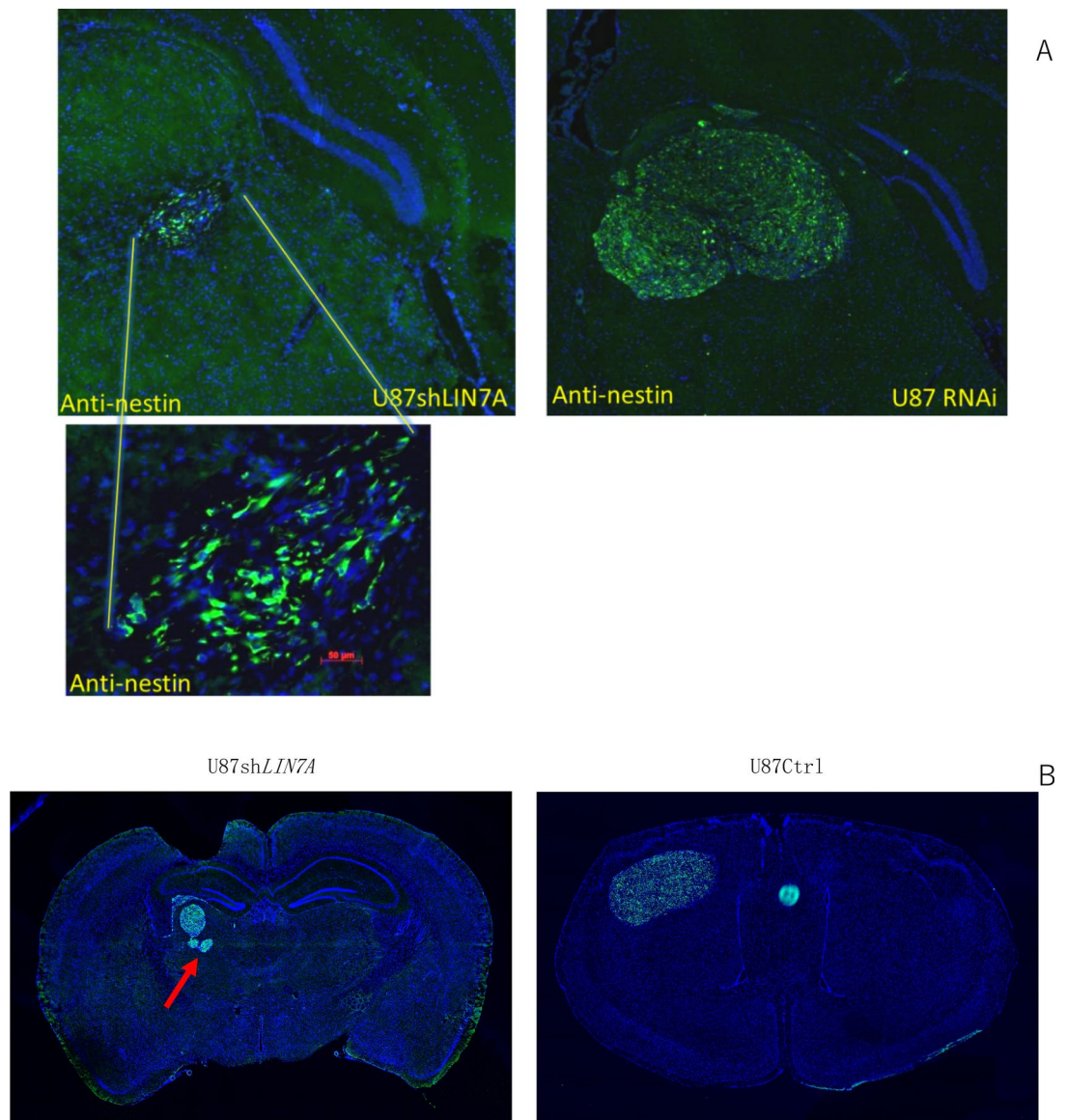
Figure 3. (continued)

Fig. 4. Observations of U87sh*LIN7A* cell growth pattern changes in an intracranial model. (**A**) Immunofluorescence of brain tissue sections at 3 weeks post-implantation: immunofluorescence images of brain tissue sections from mice implanted intracranially with U87 cells for 3 weeks were captured. The left image shows U87sh*LIN7A* cells forming small, non-clumpy tumor lesions with loosely arranged tumor cells at higher magnification, along with numerous dispersed tumor cells at the lesion periphery. In contrast, the right image displays U87Ctrl cells forming large, clumpy tumor lesions with distinct marginal boundaries and few invasive tumor cells. (**B**) Immunofluorescence of brain tissue sections at 4 weeks post-implantation: At 4 weeks post-implantation, immunofluorescence images of brain sections showed that the volume of tumor lesions in U87sh*LIN7A* mice remained smaller compared to U87Ctrl. Additionally, numerous disseminated satellite foci were observed in close proximity to the primary tumor mass (red arrows), indicating increased invasiveness of the U87Ctrl tumors.
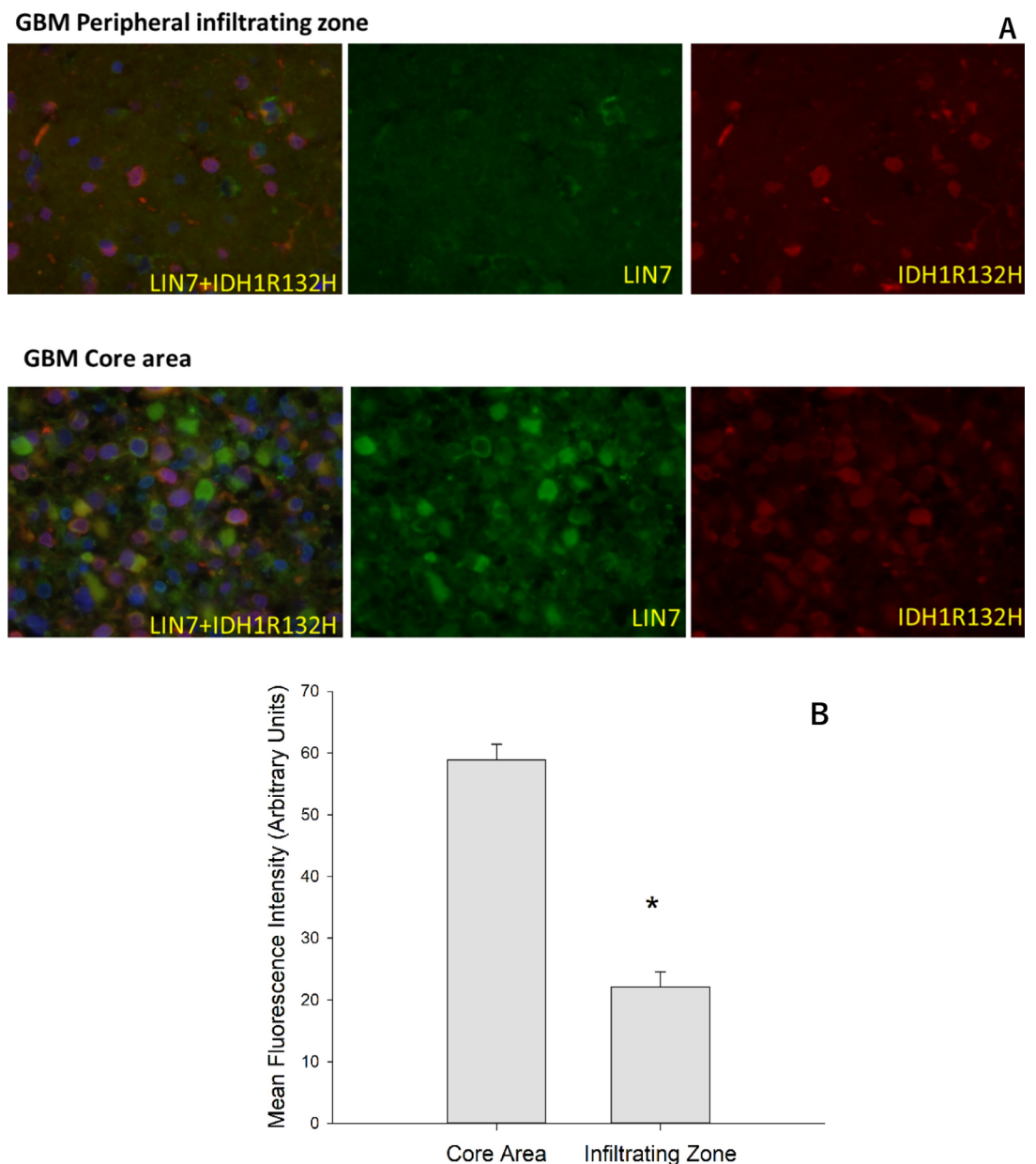
Fig. 5. Immunofluorescence analysis of clinical tumor tissue samples. (**A**) LIN7A Expression in clinical glioblastoma tissue sample: Fluorescence signals for IDH1R132H (red, right column) and LIN7A protein (green, middle column) were captured and analyzed using ImageJ software. The fluorescence images showed that LIN7A expression was more concentrated in the core region of the tumor compared to the infiltrating area, indicating a potential regional variation in LIN7A expression within the tumor. (**B**) Quantitative analysis of LIN7A expression across five clinical cases: five clinical tumor tissue samples were analyzed to quantify the expression levels of LIN7A. Statistical analysis confirmed a significant difference in LIN7A expression between the core and infiltrating areas, with the core region showing higher LIN7A levels (*$P < 0.01$).
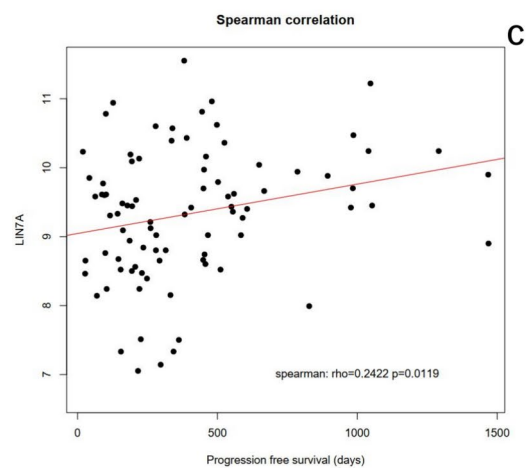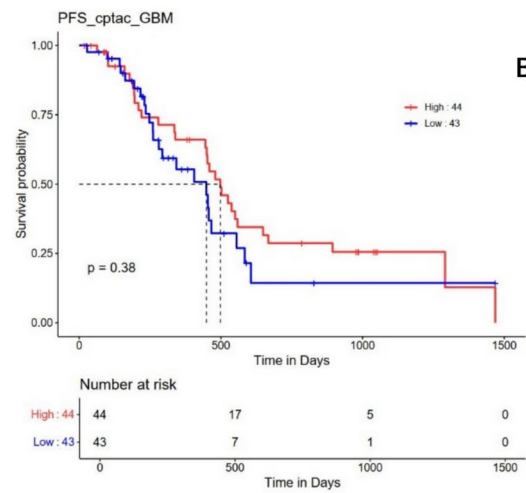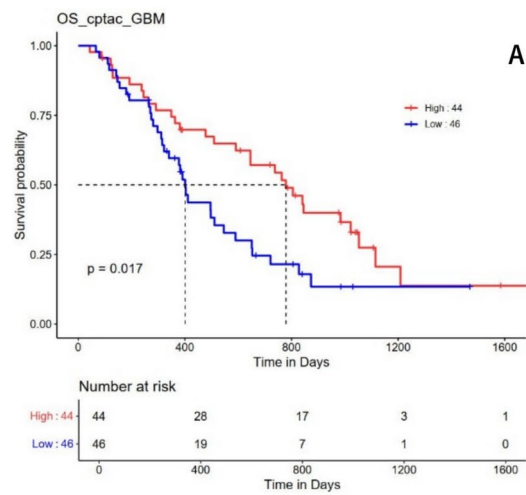
◄**Fig. 6**. The expression of *LIN7A* gene as a prognostic indicator. (**A**) Kaplan–Meier curve analysis for overall survival: Kaplan–Meier curve analysis revealed a statistically significant difference in median survival time between the high and low *LIN7A* expression groups, with median survival times of 779 days and 401 days, respectively ($P < 0.05$). The survival curves for high (blue) and low (red) *LIN7A* expression groups are shown, with the difference in survival times indicating the prognostic value of *LIN7A* expression in overall survival. Blue line represents the low *LIN7A* expression group. Red line represents the high *LIN7A* expression group. (**B**) Kaplan–Meier curve analysis for progression-free survival: Kaplan–Meier curve analysis showed a trend towards longer median progression-free survival time in the high *LIN7A* expression group (blue) compared to the low expression group (red). However, this difference was not statistically significant. Blue line represents the low *LIN7A* expression group. Red line represents the high *LIN7A* expression group. (**C**) Spearman correlation analysis between *LIN7A* expression and progression-free survival events: Spearman correlation analysis demonstrated a statistically significant moderate positive correlation (rho = 0.24, $P < 0.05$) between *LIN7A* expression levels and progression-free survival events, highlighting a potential link between *LIN7A* expression and tumor progression.

potentially augment the activation of the Wnt-catenin pathway, thereby facilitating the upregulation of target genes such as MMP2 and MMP9. This is a possible downstream mechanism of *LIN7A* gene silencing to promote invasion.

This study is an initial investigation into LIN7A's regulatory role in glioblastoma invasion, with limitations such as using only the U87 cell line. The animal model assessed U87 cell growth without quantitative comparison. Clinical studies had a small sample size, selecting only IDH1R132H-positive cases, resulting in non-random sampling and probably unrepresentative outcomes. Future studies could enhance by using larger samples, diverse models, and deeper analyses to understand LIN7A's involvement in glioblastoma invasion.

Conclusion
The role of *LIN7A* as a tumor suppressor gene in U87 cells is evident, as its silencing results in a notable enhancement in tumor cell aggressiveness, potentially attributed to the compromised cell junction formation, disrupted cell polarity, and heightened activity of the β-catenin pathway. Further investigation is warranted to elucidate the potential upstream and downstream mechanisms by which the LIN7A protein regulates glioblastoma cell invasion.

Data availability
The data that support the findings of this study are available from the corresponding authors on request.

References
1. Tan, A. C. et al. Management of glioblastoma: State of the art and future directions. *CA Cancer J. Clin.* **70**(4), 299–312 (2020).
2. Preusser, M. et al. Current concepts and management of glioblastoma. *Ann. Neurol.* **70**(1), 9–21 (2011).
3. Dong, Z. et al. Wnt/beta-catenin pathway involvement in ionizing radiation-induced invasion of U87 glioblastoma cells. *Strahlenther. Onkol.* **191**(8), 672–680 (2015).
4. de Groot, J. F. et al. Tumor invasion after treatment of glioblastoma with bevacizumab: radiographic and pathologic correlation in humans and mice. *NeuroOncology* **12**(3), 233–242 (2010).
5. Keunen, O. et al. Anti-VEGF treatment reduces blood supply and increases tumor cell invasion in glioblastoma. *Proc. Natl. Acad. Sci. U. S. A.* **108**(9), 3749–3754 (2011).
6. Nelson, W. J. Remodeling epithelial cell organization: transitions between front-rear and apical-basal polarity. *Cold Spring Harb. Perspect. Biol.* **1**(1), a000513 (2009).
7. Woodham, E. F. & Machesky, L. M. Polarised cell migration: intrinsic and extrinsic drivers. *Curr. Opin. Cell Biol.* **30**, 25–32 (2014).
8. Lemke, D. et al. Slowing down glioblastoma progression in mice by running or the anti-malarial drug dihydroartemisinin? Induction of oxidative stress in murine glioblastoma therapy. *Oncotarget* **7**(35), 56713–56725 (2016).
9. Nevo, I. et al. Identification of molecular pathways facilitating glioma cell invasion in situ. *PLoS One* **9**(11), e111783 (2014).
10. Paw, I. et al. Mechanisms regulating glioma invasion. *Cancer Lett.* **362**(1), 1–7 (2015).
11. Kalluri, R. & Weinberg, R. A. The basics of epithelial-mesenchymal transition. *J. Clin. Investig.* **119**(6), 1420–1428 (2009).
12. Polyak, K. & Weinberg, R. A. Transitions between epithelial and mesenchymal states: acquisition of malignant and stem cell traits. *Nat. Rev. Cancer* **9**(4), 265–273 (2009).
13. Gandalovicova, A. et al. Cell polarity signaling in the plasticity of cancer cell invasiveness. *Oncotarget* **7**(18), 25022–25049 (2016).
14. Royer, C. & Lu, X. Epithelial cell polarity: a major gatekeeper against cancer?. *Cell Death Differ.* **18**(9), 1470–1477 (2011).
15. Jung, H.-Y. et al. Apical–basal polarity inhibits epithelial–mesenchymal transition and tumour metastasis by PAR-complex-mediated SNAI1 degradation. *Nat. Cell Biol.* **21**(3), 359–371 (2019).
16. Margolis, B. The Crumbs3 polarity protein. *Cold Spring Harb. Perspect. Biol.* **10**(3), a027961 (2018).
17. Stephens, R. et al. The scribble cell polarity module in the regulation of cell signaling in tissue development and tumorigenesis. *J. Mol. Biol.* **430**(19), 3585–3612 (2018).
18. Martin, E. et al. New insights into the organization and regulation of the apical polarity network in mammalian epithelial cells. *FEBS J.* **288**(24), 7073–7095 (2021).
19. Lawson, C. D. & Ridley, A. J. Rho GTPase signaling complexes in cell migration and invasion. *J. Cell Biol.* **217**(2), 447–457 (2018).
20. Gagnoux-Palacios, L. et al. Cell polarity and adherens junction formation inhibit epithelial Fas cell death receptor signaling. *J. Cell Biol.* **217**(11), 3839–3852 (2018).
21. Monzani, E. et al. AQP1 is not only a water channel: it contributes to cell migration through Lin7/beta-catenin. *PLoS One* **4**(7), e6167 (2009).
22. Uzawa, K. et al. Suppression of metastasis by mirtazapine via restoration of the Lin-7C/beta-catenin pathway in human cancer cells. *Sci. Rep.* **4**, 5433 (2014).

23. Hu, Y. & Smyth, G. K. ELDA: extreme limiting dilution analysis for comparing depleted and enriched populations in stem cell and other assays. *J. Immunol. Methods* **347**(1–2), 70–78 (2009).
24. Scrace, S. et al. Use of the xCELLigence system for real-time analysis of changes in cellular motility and adhesion in physiological conditions. *Methods Mol. Biol.* **1046**, 295–306 (2013).
25. Vinci, M., Box, C. & Eccles, S. A. Three-dimensional (3D) tumor spheroid invasion assay. *J. Vis. Exp.* **99**, e52686 (2015).
26. Boutron, I. et al. Reporting animal research: Explanation and elaboration for the ARRIVE guidelines 2.0. *PLOS Biol.* **18**(7), e3000411 (2020).
27. Flecknell, P. A. Anaesthesia of animals for biomedical research. *Br. J. Anaesth.* **71**(6), 885–894 (1993).
28. Bland, J. M. & Altman, D. G. Survival probabilities (the Kaplan-Meier method). *BMJ* **317**(7172), 1572 (1998).
29. Vasaikar, S. V. et al. LinkedOmics: analyzing multi-omics data within and across 32 cancer types. *Nucleic Acids Res.* **46**(D1), D956–D963 (2018).
30. Li, P. et al. Epithelial cell polarity determinant CRB3 in cancer development. *Int. J. Biol. Sci.* **11**(1), 31–37 (2015).
31. Buckley, C. E. & Johnston, D. S. Apical–basal polarity and the control of epithelial form and function. *Nat. Rev. Mol. Cell Biol.* **23**(8), 559–577 (2022).
32. Gandalovičová, A. et al. Cell polarity signaling in the plasticity of cancer cell invasiveness. *Oncotarget* **7**(18), 25022–25049 (2016).
33. Ellenbroek, S. I., Iden, S. & Collard, J. G. Cell polarity proteins and cancer. *Semin. Cancer Biol.* **22**(3), 208–215 (2012).
34. Harris, B. Z., Venkatasubrahmanyam, S. & Lim, W. A. Coordinated folding and association of the LIN-2, -7 (L27) domain. *J. Biol. Chem.* **277**(38), 34902–34908 (2002).
35. Halaoui, R. & McCaffrey, L. Rewiring cell polarity signaling in cancer. *Oncogene* **34**(8), 939–950 (2014).
36. Ribatti, D., Tamma, R. & Annese, T. Epithelial-mesenchymal transition in cancer: A historical overview. *Transl. Oncol.* **13**(6), 100773 (2020).
37. Kyuno, D. et al. Role of tight junctions in the epithelial-to-mesenchymal transition of cancer cells. *Biochim. Biophys. Acta Biomembr.* **1863**(3), 183503 (2021).
38. Luo, C. et al. microRNA-501-3p suppresses metastasis and progression of hepatocellular carcinoma through targeting LIN7A. *Cell Death Dis.* **9**(5), 535 (2018).
39. Gruel, N. et al. LIN7A is a major determinant of cell-polarity defects in breast carcinomas. *Breast Cancer Res.* https://doi.org/10.1186/s13058-016-0680-x (2016).
40. Lemke, D. et al. Primary glioblastoma cultures: can profiling of stem cell markers predict radiotherapy sensitivity?. *J. Neurochem.* **131**(2), 251–264 (2014).
41. Martin, T. A., Mason, M. D. & Jiang, W. G. Tight junctions in cancer metastasis. *Front. Biosci.* **16**(3), 898–936 (2011).
42. Giepmans, B. N. & van Ijzendoorn, S. C. Epithelial cell-cell junctions and plasma membrane domains. *Biochim. Biophys. Acta* **1788**(4), 820–831 (2009).
43. Garcia, M. A., Nelson, W. J. & Chavez, N. Cell–cell junctions organize structural and signaling networks. *Cold Spring Harb. Perspect. Biol.* **10**(4), a029181 (2018).
44. Shin, K., Fogg, V. C. & Margolis, B. Tight junctions and cell polarity. *Annu. Rev. Cell Dev. Biol.* **22**, 207–235 (2006).
45. Yu, S., He, J. & Xie, K. Zonula occludens proteins signaling in inflammation and tumorigenesis. *Int. J. Biol. Sci.* **19**(12), 3804–3815 (2023).
46. Liu, J. et al. Wnt/β-catenin signalling: function, biological mechanisms, and therapeutic opportunities. *Signal Transduct. Target. Ther.* https://doi.org/10.1038/s41392-021-00762-6 (2022).
47. Perego, C. et al. Invasive behaviour of glioblastoma cell lines is associated with altered organisation of the cadherin-catenin adhesion system. *J. Cell Sci.* **115**(Pt 16), 3331–3340 (2002).
48. Perego, C. et al. Mammalian LIN-7 PDZ proteins associate with beta-catenin at the cell-cell junctions of epithelia and neurons. *EMBO J.* **19**(15), 3978–3989 (2000).
49. Onda, T. et al. Lin-7C/VELI3/MALS-3: an essential component in metastasis of human squamous cell carcinoma. *Cancer Res.* **67**(20), 9643–9648 (2007).

Author contributions

All authors have significantly contributed to this manuscript. Xiaojuan Lyu: conceptualization, funding acquisition, formal analysis (lead), project administration, writing—original draft. Yuxiang Shi: investigation (equal). Daixu Wang: methodology (lead), investigation (equal). Xing Cao: resources, methodology (supporting). Jipeng Guo: investigation (equal). Guodong Huang: investigation (equal). Lin Zhou: visualization, formal analysis (supporting). Mengxian Zhang: funding acquisition, methodology (supporting) Zhen Dong: supervision, writing – review & editing. All authors read and approved the final manuscript.

Declarations

Competing interests

The authors declare no competing interests.

Additional information

Supplementary Information The online version contains supplementary material available at https://doi.org/10.1038/s41598-025-91285-5.

Correspondence and requests for materials should be addressed to Z.D.

Reprints and permissions information is available at www.nature.com/reprints.

Publisher's note Springer Nature remains neutral with regard to jurisdictional claims in published maps and institutional affiliations.